JACS
JOURNAL OF THE AMERICAN CHEMICAL SOCIETY
Article
pubs.acs.org/JACS

One-Step Hydrothermal Synthesis of Manganese-Containing MFI-Type Zeolite, Mn−ZSM-5, Characterization, and Catalytic Oxidation of Hydrocarbons

Yongtao Meng,[†] Homer C. Genuino,[†] Chung-Hao Kuo,[†] Hui Huang,[†] Sheng-Yu Chen,[†] Lichun Zhang,[‡] Angelo Rossi,[†] and Steven L. Suib*[,†,‡]

[†]Department of Chemistry and [‡]Institute of Materials Science, University of Connecticut, Storrs, Connecticut 06269-3060, United States

Supporting Information

ABSTRACT: Manganese-containing MFI-type Mn−ZSM-5 zeolite was synthesized by a facile one-step hydrothermal method using tetrapropylammonium hydroxide (TPAOH) and manganese(III)-acetylacetonate as organic template and manganese salts, respectively. A highly crystalline MFI zeolite structure was formed under pH = 11 in 2 days, without the need for additional alkali metal cations. Direct evidence of the incorporation of Mn in the zeolite framework sites was observed by performing structure parameter refinements, supported by data collected from other characterization techniques such as IR, Raman, UV−vis, TGA, N_2-adsorption, SEM, TEM, EDAX, and XPS. UV−vis spectra from the unique optical properties of Mn−ZSM-5 show two absorption peaks at 250 and 500 nm. The absorption varies in different atmospheres accompanied by a color change of the materials due to oxygen evolution. Raman spectra show a significant and gradual red shift from 383 cm^{-1} to 372 cm^{-1} when the doping amount of Mn is increased from 0 to 2 wt %. This suggests a weakened zeolite structural unit induced by the Mn substitution. The catalytic activity was studied in both gas-phase benzyl alcohol oxidation and toluene oxidation reactions with remarkable oxidative activity presented for the first time. These reactions result in a 55% yield of benzaldehyde, and 65% total conversion of toluene to carbon dioxide for the 2% Mn−ZSM-5. Temperature programmed reduction (TPR) using CO in He demonstrates two reduction peaks: one between 300 and 500 °C and the other between 500 and 800 °C. The first reduction peak, due to manganese-activated oxidation sites shifted from higher temperature to lower temperature, and the peak intensity of CO_2 rises when the dopant amount increases. For the first time, calculated photophysical properties of a model $Mn(O\text{-}SiH_3)_4^-$ compound, an Mn-embedded zeolite cluster, and model Mn oxides help to explain and interpret the diffuse reflectance spectroscopy of Mn−ZSM-5 zeolites.

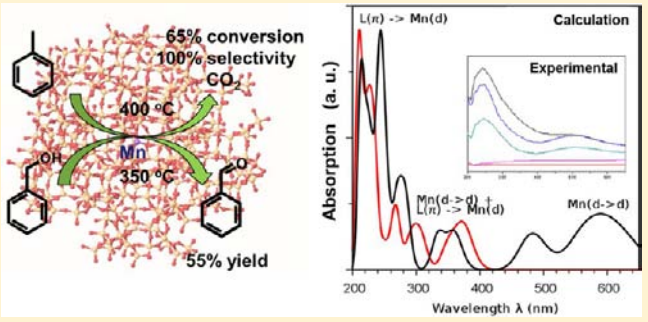

INTRODUCTION

Transition metal (TM) doped zeolites have been widely studied due to their novel catalytic application in oxidation reactions, such as benzene oxidation to phenol, methane oxidation to methanol and catalytic decomposition of NO and N_2O.[1] Among these doped zeolites, Cu and Fe containing ZSM-5 zeolites were given more attention because of their high activities due to the alpha-oxygen on the peroxo-bridged binuclear TM sites which were formed by activation under NO_x or O_2.[2,3] A moderate temperature below 350 °C is needed to achieve the selective conversion from methane to methanol or from NO_x to N_2. N_2O is found to be the only species that could form alpha-O, rather than O_2, which is the active site for selective oxidation. In addition, the transition metal is present not only as a surface active site, but also as a framework substituted site. Titanium containing MFI type microporous silicates (TS-1) were found to be good catalysts for mild epoxidation of olefins, hydroxylation of aromatics, and oxidation of alcohols and amines, etc., using H_2O_2 as an oxidant.[4−7] Other transition metal-doped MFI- and MEL-type zeolites, such as vanadium, iron, and chromium substituted in framework Si^{4+} in silicalite-1 (ZSM-5) and silicalite-2 (ZSM-11), have also been synthesized.[8−10] Most of these catalysts were applied in selective oxidation reactions with the use of H_2O_2 or TBHP as oxidants.

Manganese oxides, particularly octahedral molecular sieves (OMS-2) have been extensively studied as superior oxidation catalysts in alcohol oxidation and as catalysts in decomposition of volatile organic compounds (VOCs) due to their high activity on account of mixed valent properties.[11] However, their thermal stability is not as good as traditional aluminosilicate zeolites due to phase changes or poisoning by moisture.[11d,12] Zeolites or aluminosilicates have been used in different

Received: February 11, 2013
Published: May 16, 2013

   dx.doi.org/10.1021/ja4013936 | J. Am. Chem. Soc. 2013, 135, 8594−8605

applications, such as adsorption, ion-exchange, and petrorefining because of their notable stability and adjustable acid sites of high activity.[13] Manganese-substituted silicates have not been fully studied with respect to both their structure and catalytic properties.[9,14,15] Direct evidence of the existence of Mn in the framework is still needed, and only a few redox properties of manganese-containing zeolite have been reported.[15] For preparation, a facile synthesis method is needed to replace the present methods by using harsh acid hydrofluoride,[16] or recrystallization of Mn(II)-exchanged magadiite.[17] Although a hydrothermal synthesis method has been reported using manganese acetate under a pH = 13, a possible precipitation problem may remain. In addition, the products formed have no redox sites based on CO adsorption of reduced and oxidized samples.[18]

Here, we report a facile synthesis of a Mn-containing MFI-type zeolite, Mn−ZSM-5, by hydrothermal synthesis from a clear solution made with a manganese organic precursor and silicates under mild conditions at pH =11. Full characterization was performed by various spectroscopic techniques, including UV−vis, IR, Raman, and X-ray diffraction, SEM, and TEM where direct evidence of framework manganese has been found (vide infra). The synthesized Mn−ZSM-5 shows considerable activity as a catalyst in the conversion of benzyl alcohol to benzaldehyde with 55% yield, and toluene total oxidation to carbon dioxide with 65% conversion. Such a high activity of Mn−ZSM-5 has been ascribed to the well-isolated Mn species as an excellent oxygen carrier and donor substituted in the zeolite framework and bonded to the surface. This is the first time a highly loaded Mn−ZSM-5 has been synthesized in one step and found to be an appropriate catalyst in two different selective oxidation processes. The computational results presented here attempt to establish a correlation between the experimental UV−vis of Mn-containing ZSM-5 zeolites and calculated spectra toward achieving a better understanding of the nature of Mn−ZSM-5 interactions.

EXPERIMENTAL SECTION

Synthesis of All Silica ZSM-5 Zeolites. All silica ZSM-5 zeolites were prepared as described elsewhere.[19] In a typical synthesis, 25 g of tetraethylorthosilicate (TEOS, Aldrich, 98%) was added dropwise to 25 g distilled deionized water (DDW) with stirring for a half an hour, followed by adding 30 g TPAOH (Sigma Aldrich, 1.0 M) aqueous solution as a structure-directing agent (SDA) dropwise using a buret. The well-mixed solution (solution A) was stirred for 3 h, 50 mL of which was measured and added into an autoclave with a Teflon liner. The charged autoclave was put into an oven held at 180 °C for a hydrothermal reaction. The hydrothermal reaction could be performed from two days to more than ten days to get well-crystallized products; here we did all the syntheses for 48 h. After the reaction, the autoclave was cooled and the white products were collected, filtered, and washed 5 times with DDW, dried overnight at 120 °C and calcined at 550 °C. The temperature for calcinations was increased using a ramp of 2 °C min^{-1} from room temperature to 550 °C, then keep at 550 °C for 5 h, in order to remove all the organic solvents and SDA. The final product is denoted as Si−ZSM-5, which stands for an all silica ZSM-5 without any aluminum ions.

Synthesis of Mn−ZSM-5 Zeolites. In a typical synthesis of Mn−ZSM-5, e.g. 2 wt % Mn−ZSM-5, 0.44 g manganese(III)-acetylacetonate (Sigma Aldrich) was fully dissolved in 20 mL ethanol (Pharmco Aaper, Absolute). This solution was added dropwise into half of the aforementioned solution A before being placed into the autoclave and stirred for 3 h to obtain well-dissolved manganese-containing solution (solution B), which has a transparent, red-wine color. Fifty milliliters of the solution B was charged into the autoclave, and the same hydrothermal treatment was performed as aforementioned. The products were filtered, and washed 5 times with DDW, dried, and calcined. After being calcined, the products showed a pale-pink color and are denoted as Mn−ZSM-5. All the synthesized ZSM-5 materials in this study are aluminum free with the goal of exploring only the effect of adding manganese on the properties of these newly formed zeolites.

CHARACTERIZATION

Structure Analysis by X-ray Diffraction. XRD data were collected on a Rigaku UltimaIV instrument using Cu Kα radiation at a beam voltage of 40 kV and a 45 mA beam current.

Spectroscopic Studies by FT-IR, UV−vis and Raman. FT-IR spectra were taken from pressed pellets with KBr diluted zeolite samples on a Thermo Scientific Nicolet 8700 spectrometer with a 4 cm^{-1} resolution. CaF_2 windows were used; dry N_2 was purged into the cell and passed through to eliminate all the moisture and CO_2 absorbed on the samples before each test. Diffuse-reflectance UV−vis spectra were collected using a Shimadzu UV-2450 UV−vis spectrophotometer in a 200 nm to ∼800 nm range. For each test, a 0.2 g solid sample was diluted by 2 g $BaSO_4$. The Raman spectra were taken on a Renishaw 2000 Raman microscope, which includes an optical microscope and a CCD camera for multichannel detection.

Morphology (SEM, TEM). High-resolution scanning electron microscope photographs were taken on a Zeiss DSM 982 Gemini field-emission scanning microscope (FESEM) to get morphological information. A high-resolution transmission electron microscope (HRTEM) was used to characterize the crystallized structure and the morphology of the samples by using a JEOL 2010 instrument with an accelerating voltage of 200 kV.

Elemental and Surface Analysis (EDXS, XPS). Elemental analysis was performed using a JEOL 2010 instrument equipped with energy dispersive X-ray spectroscopy (EDXS). Surface analysis was done on a PHI model 590 spectrometer with multiprobes (ΦPhysical Electronics Industries Inc.), using Al Kα radiation (λ = 1486.6 eV) as the radiation source. The powder samples were pressed on carbon tape mounted on adhesive copper tape stuck to a sample stage placed in the analysis chamber.

N_2 Adsorption/Desorption and Specific Surface Area. The adsorption and desorption isotherms were measured on a Micrometritics ASAP 2010 instrument. Samples were predegassed at 300 °C for 6 h prior to each measurement in order to remove water and other adsorbed species. The isotherms of adsorption and desorption were measured at relative pressures (P/P_0) from 0.001 to 0.995 and from 0.995 to 0.001, respectively.

Thermogravimetric Analysis (TGA). TGA was performed on Hi-Res TGA 2950 Thermogravimetric Analyzer in both N_2 and O_2 atmospheres.

Temperature-Programmed Reduction (TPR). TPR mass spectrometry experiments were conducted using a Thermolyne 79300 model tube furnace equipped with an e-Vision + residual gas analyzer MKS coupled with a quadruple mass selective detector. In a typical test, a 200 mg of catalyst was loaded in the middle of a quartz tubular reactor, with quartz wool supports on both sides. First, the catalyst was cleaned by flowing helium at a rate of 50 cm^3 min^{-1} (sccm) for one hour at 180 °C, and second, cooled to room temperature. During the test, the catalyst was heating at 10 °C min^{-1} to 800 °C in a 3% (V/V) CO−He mixture at a flow rate of 60 mL/min.

Catalytic Test. Gas-phase catalytic toluene oxidation was used as a probe reaction to detect the oxidation active sites of the Mn-containing zeolite. The reaction was carried out in a quartz tubular fixed-bed flow reactor (i.d., 4 mm) under atmospheric pressure. The reactor was put into an electric tubular furnace coupled with a controller to control the temperature, with a K-type thermocouple plugged into the catalyst bed. Typically, 100 mg of catalyst was packed in the middle of the reactor supported by glass wool at both sides. Before the reaction, the catalyst was pretreated by heating at 200 °C under a continuous UHP helium flow for 2 h. The catalytic reaction

dx.doi.org/10.1021/ja4013936 | J. Am. Chem. Soc. 2013, 135, 8594−8605

was done by bubbling ultra zero grade air (21 vol % O_2) as the reaction gas into a 200 mL anhydrous toluene solution at a constant flow rate of 20 sccm controlled by a MKS mass flow controller. The reaction temperature varied from 100 to 420 °C. Sampling of the gas-phase product was carried out at least 20 min after the temperature reached the desired value. The effluent gas products were passed through a cold trap (dry ice) before entering a SRI 8610C gas chromatography (GC) to analyze the gas components (O_2, N_2, CO, and CO_2). Liquid products from the cold trap were extracted, dehydrated, and analyzed by GC-Mass (HP 5890A, with an HP 5871 series mass detector). Under present reaction conditions, incomplete oxidation products were not found (Figure S1 in Supporting Information [SI]). Thus the conversion was calculated based on the O_2 consumed during the oxidation process by using the equation from our former paper.[20]

The gas-phase benzyl alcohol oxidation reaction was performed as another representative reaction. The reaction was carried out in a homemade fixed-bed flow system, which included a quartz reactor (L = 430 mm, i.d. = 10 mm) placed in a temperature controllable tubular furnace (Thermal Scientific, Lindberg Blue M). Two hundred milligrams of catalyst was loaded in the middle of the reactor with glass wool and glass beads held on both sides. Before the reaction, the catalyst was activated under N_2 and O_2 flow (1:1.6, V/V) for 2 h at a desired reaction temperature. The liquid benzyl alcohol was charged by a syringe pump at a rate of 0.02 mL/min, and passed through a constantly preheated steel tube (220 °C) to vaporize before it running into the reactor. The vaporized gas-phase benzyl alcohol was continuously transported by the gas flow (N_2/O_2, 1:1.6) through the catalyst, the effluents were collected by a cold trap (dry ice), and the gas phase was detected by on-line SRI 8610C gas chromatography (GC) to detect any total oxidation products, mainly CO or CO_2, and these products were only found when the reaction temperature increased above 350 °C. The liquid products were dehydrated by $MgSO_4$ and diluted with acetone (1 μL products/1 mL acetone); for each sample, 1 μL of 1-decane was added as internal standard and the sample analyzed by HP 5890 series II GC equipped with a MTX-biodiesel TG w/Integra-Gap capillary column (14.0 m × 530 μm × 0.16 μm) with an FID detector. The yield was calculated on the basis of the standard curve (Figure S5 in SI) made by analysis of benzyl alcohol and benzaldehyde mixtures of a concentration gradient (20–100%, mol/mol).

Computational Details. Calculations were performed by utilizing the Gaussian[21] and GAMESS[22] programs where the excitation energies were calculated using time dependent density functional theory.[23] The hybrid B3LYP exchange functional[24] was employed throughout all the calculations. The choice of model systems is not easy, especially for ZSM-5 zeolites where the structure is quite complex. In these studies, the structure of Mn–ZSM-5 was represented by smaller model compounds to reduce the complexity and computational cost. The model compounds were chosen to ensure that ligands attached to the Mn ion will affect the local environment of the Mn center to provide reasonable information about the experimental electronic spectra. The Mn and O bonding ligands that were used in the calculations include $H_3Si–O^-$, as shown in Figure 1, $H_3Si–O–SiH_3$, and $H_3Si–O–SiH_2–O–SiH_3$. Both four- and six-coordinate framework bonding sites were explored.

In addition isolated model complexes of MnO_4^{x-} and MnO_6^{x-} were employed in an attempt to obtain information about the possible existence of extra-framework sites for Mn. In some cases, a complete optimization of the model cluster was performed, although this approach is fraught with uncertainty, because a framework Mn ion will be more constrained than in a cluster. In other situations, reasonable model geometries were used to observe trends in the spectra. In the case of Mn oxides, no optimizations were performed, and only fixed bond distances and angles based on experimental values were used. In all cases, if the model complex was charged, either positively or negatively, then point charges of opposite sign were positioned around the model complex to provide a compensating charge of equal magnitude and yielding charge neutrality. For these calculations, the

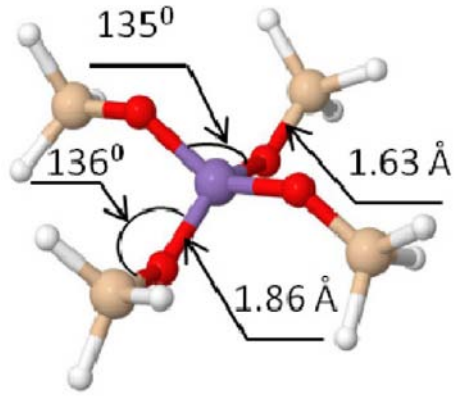

Figure 1. Model $Mn(OSiH_3)_4^-$ compound with optimized geometric parameters. The atoms are colored with respect to atom type with Mn as violet, oxygen as red, silicon as light brown, and hydrogen as white.

LANL2DZ basis set[25] was used for the Mn atom, and the 6-31G(d) basis[26] for all ligand atoms (H, O, or Si).

A limited validation of the cluster model was performed by inserting a Mn ion into the metal–zeolite framework (MZF) and using hybrid quantum mechanics/molecular mechanics (QM/MM) to study electronic effects of the local framework surrounding the Mn ion. The embedded-cluster approach employing a two-layer ONIOM[27] system was used to obtain optimized geometries and excitations. In the present work, the electronic structure of an Mn ion plus four $-O-SiH_2^-$ ligands are designated the primary structure (PS) and are treated quantum mechanically (QM). For these calculations, the TZVP basis[28] and 6-31G(d) basis[26] were used for the Mn atom and ligand atoms, respectively. Twelve hydrogen link atoms were used to saturate dangling Si bonds between the PS and the secondary subsystem (SS). The remaining atoms of ZSM-5, i.e. the SS, are treated with molecular mechanics (MM) where UFF[29] parameters are used. The embedded cluster model is shown in Figure 2.

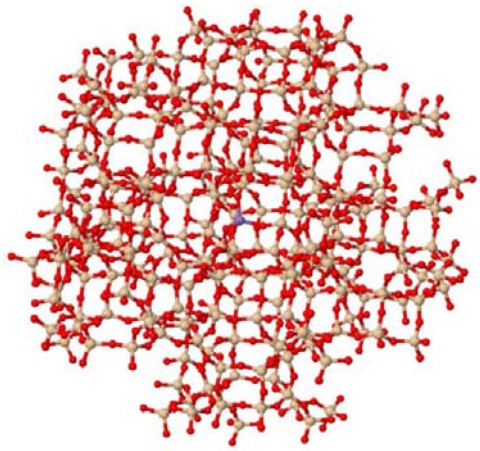

Figure 2. Embedded Mn–zeolite cluster $Mn(OSiH_2)_4Si_{155}O_{591}$. It is important to emphasize that terminal oxygen atoms were not capped which could have an influence on the overall structure of the cluster.

RESULTS

X-ray Diffraction (XRD). The XRD patterns indicate the synthesized material is well crystallized, as shown in Figure 3. The narrow peak widths suggest a relatively large particle size, which is around 500 nm, as confirmed by FESEM and TEM. All of the peaks match the standard phase of ZSM-5 zeolite, whereas slight shifting of the peak to a smaller angle was

dx.doi.org/10.1021/ja4013936 | J. Am. Chem. Soc. 2013, 135, 8594–8605

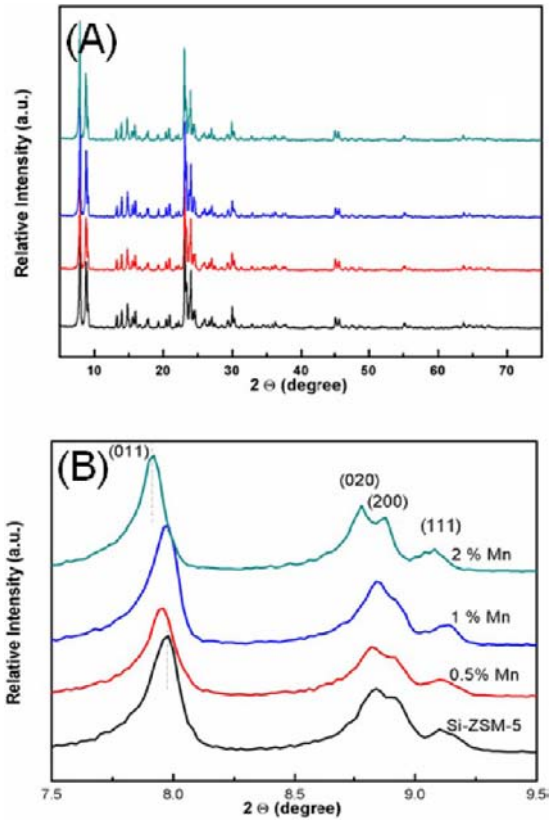

Figure 3. (A) Wide-angle XRD patterns and (B) enlarged scale between 2θ = 7.5 and 9.5 of (A), from bottom to top: Si−ZSM-5, 0.5 wt % Mn−ZSM-5, 1 wt % Mn−ZSM-5 and 2 wt % Mn−ZSM-5.

observed for manganese-containing materials, 0.5% Mn−ZSM-5 (0.02 degree) and 2% Mn−ZSM-5 (0.06°) compared with the all silica ZSM-5 zeolite, which implies substitution of smaller tetrahedrally coordinated Si atoms (0.4 Å in crystal form) with heteroatoms Mn (II or III) which have a larger size (0.5−1.0 Å) as ions in a crystalline environment, yielding an increased lattice parameter value.

Scanning Electron Microscopy (SEM) and Transmission Electron Microscopy (TEM). Figure 4 shows the typical morphologies of synthesized Si−ZSM-5 and Mn-containing ZSM-5 zeolite, which is composed of single crystals of intergrown hexagonal platelets having an evenly distributed particle size between 300 and 500 nm. Each particle was proven to be a single crystal as determined by selected area electron diffraction (SAED) patterns of TEM experiments taken at different crystalline orientations (Figure 5).

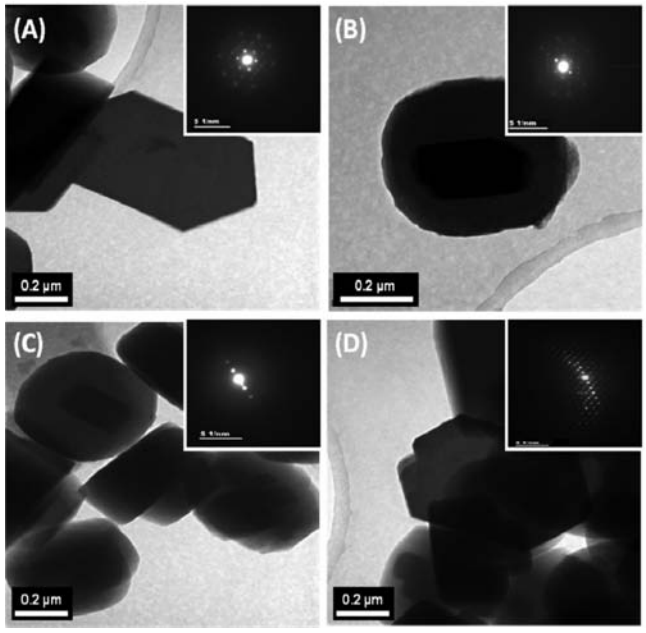

Figure 5. Representative TEM images of 0.5% Mn−ZSM-5, and corresponding SAED patterns.

Surface Area, Porosity, and Energy Dispersive X-ray Spectroscopy (EDXS). N_2 adsorption−desorption isotherms are measured and show a typical microporous feature of such materials (type-I isotherm). The results summarized in Table 1 show the BET specific surface area remains similar in terms of

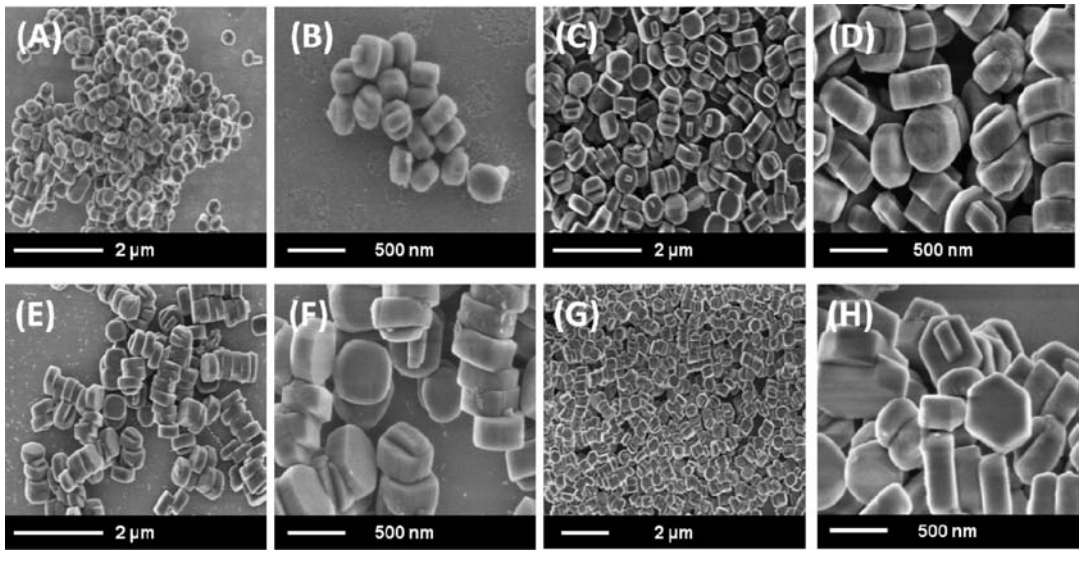

Figure 4. SEM images of Mn−ZSM-5 of different Mn contents, A, B (Si−ZSM-5), C, D, (0.5%) ; E, F(1%); G,H (2%).

dx.doi.org/10.1021/ja4013936 | J. Am. Chem. Soc. 2013, 135, 8594−8605

Table 1. Physiochemical Properties of Mn−ZSM-5 Materials

samples (%)	BET surface area[a] [m²/g]	vol[b] [cm³/g]	EDXS Si/Mn nom.[c]	EDXS Si/Mn exp[d]	XPS Si/Mn
all Si	316 (26)	0.11	0	0	0
0.5	323 (9)	0.11	183.0	330.7	98.4
1	318 (14)	0.11	91.5	122.0	63.2
2	325 (17)	0.13	45.8	(168.6) 27.7[e]	48.4

[a]Standard deviation. [b]Micropore volume determined by *t*-plot method. [c]Nominal molar ratio of Si to Mn. [d]Experimental molar ratio of Si to Mn determined by EDXS. [e]Analysis performed on large aggregation of particles.

increasing the Mn amount in the sample. Likewise, the micropore volume matches well without displaying any drop for doped samples. Therefore, the results reveal that the manganese in the Mn-containing ZSM-5 material is well dispersed, either in the framework or on the surface of the material, and the micropores were thus not blocked.

EDXS was used to analyze the concentration of each element in the bulk material. The Si-to-Mn molar ratio is of more interest. The experimental values of Si/Mn decrease with an increasing amount of Mn added in the initial synthesis solution. The XPS values of Si/Mn are all lower than they were from the EDXS analysis which means there is more surface manganese than in the bulk material. Considering different depths of both techniques in detecting element concentrations, XPS measures at about 40 Å depth, whereas EDXS penetrates from tens of nanometers to hundreds of nanometers. For the 0.5% sample, the surface Si/Mn = 98 which is only half as large as the nominal ratio of 183, indicating Mn accumulates on the surface. However, by increasing the Mn amount, this ratio decreases and is closer to the nominal value which could lead to an excellent substituted material. This is because homogeneous substitution happens throughout the material at a proper higher concentration, 2 wt % Mn in this case, and allows this material to potentially become an active catalyst.

Raman Spectroscopy. Raman is a sensitive technique which can detect subtle phase information, e.g. framework metal sites in zeolite and extra-framework species. Therefore, Raman was used to study the effect of adding manganese in the framework of ZSM-5 zeolite with excitation laser beams of both 544 and 488 nm (Figure 6). A well-resolved peak was observed between 372 cm^{-1} and 385 cm^{-1} for all the zeolite materials with or without manganese, which is ascribed to the characteristic vibrations of the Si−O bonds in the five-membered ring of the MFI-type unit structure. The position of this peak shifted to lower wave numbers (red shift) as the amount of manganese increased from 0% to 2%, with a peak shift from 383 cm^{-1} to 375 cm^{-1} along with broadening and lower intensity. The other characteristic peak at 803 cm^{-1} was also broadened along with weakened intensity. There were new peaks at 560 cm^{-1} and 628 cm^{-1} showing up gradually as more manganese was added. The two most intensive broad peaks arose from the 2% Mn added sample. These new peaks can be assigned to bending and symmetric stretching vibrations of framework Mn−O−Si analogous to the Ti−O−Si vibration in the TS-1 zeolite.[5] Another plausible explanation could be due to Mn−O symmetric stretching vibration from the extra manganese oxide phase (544 cm^{-1}, 648 cm^{-1}) as previously reported.[30,31] Finally, a $[Mn_2O]^{2+}$ species is also possible, since

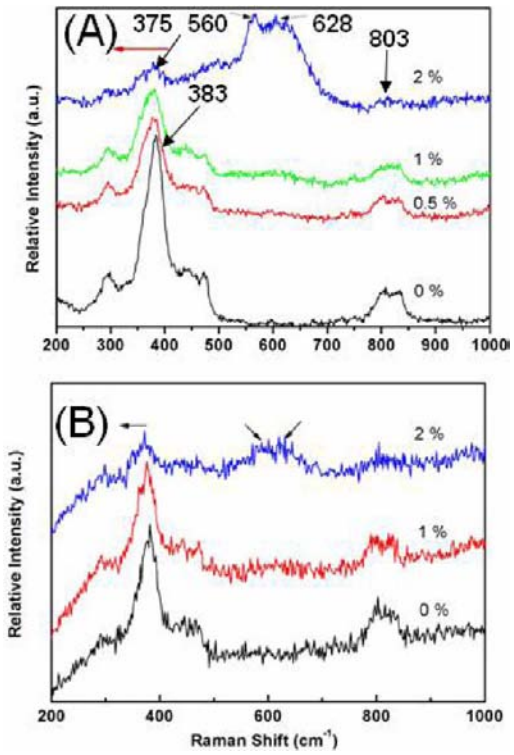

Figure 6. Raman spectra of Mn−ZSM-5 (all silica, 0.5%, 1% and 2%), taken by (A) 544 nm and (B) 488 nm laser beam.

a μ-oxo-bridged $[Cu_2O]^{2+}$ species is formed on the ZSM-5, having Raman bands at 456 cm^{-1} (symmetric) and 870 cm^{-1} (antisymmetric) as reported by Smeets et al.[32,33]

The spectra taken by 488 nm laser beam has confirmed the same shift and newly evolving bands except for the 0.5% Mn−ZSM-5, where impurities gave rise to fluorescence[5] and prevented the observation of Raman spectra. Raman spectra of different particles for the 2% Mn−ZSM-5 sample were collected (Figure S2 in SI). Different relative peak intensities of 375, 560, and 628 cm^{-1} were observed, indicating an impure material since some of the manganese might be present in a separate phase. Moreover, the intensity of peaks between 550 cm^{-1} and 650 cm^{-1} was largely eliminated due to the reduced resonance effects in this area by using the λ_{ex} = 488 nm (Figure S3 in SI).

Infrared Spectroscopy. Several characteristic vibration peaks of MFI-type zeolite material have been found in the infrared spectra (Figure 7). The well-defined peaks reveal the good crystalline property of these materials.

The absorption at 550 cm^{-1} is typically due to the pentasil framework variation and was used as a measurement of the crystallinity of this type of material. The absorption peak at 800 cm^{-1} is due to Si−O−Si symmetric stretching, while absorption peaks at 1100 cm^{-1} and 1230 cm^{-1} are assigned to asymmetric stretching of Si−O−Si, and are broadened when substitution with Mn is increased. The absorption at around 1000 cm^{-1} of Si−ZSM-5 does not appear, which may be due to largely diminished Si−OH groups caused by calcination and compression under high pressure during the sample preparation and notably is not present for the Mn−ZSM-5 materials either. This is rationalized for the same reason. However, this may also result from the substitution of OH group with manganese clusters on the surface.[34]

dx.doi.org/10.1021/ja4013936 | J. Am. Chem. Soc. 2013, 135, 8594−8605

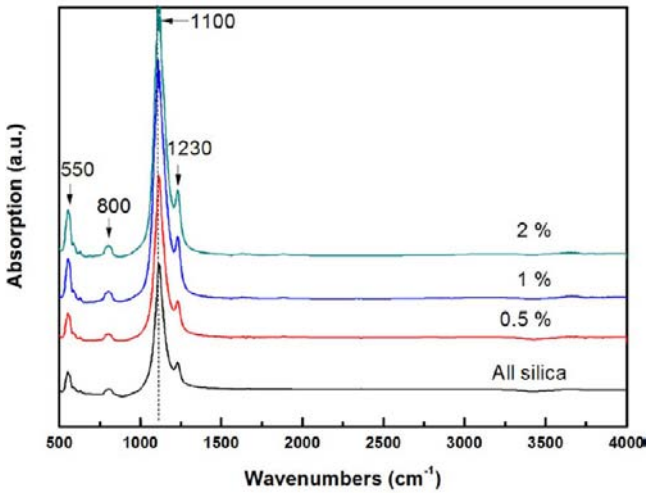

Figure 7. FT-IR spectra of Mn−ZSM-5 (all silica, 0.5%, 1%, and 2%).

UV−Vis Spectroscopy. The UV−visible spectra are shown in Figure 8. As the amount of manganese is increased, the

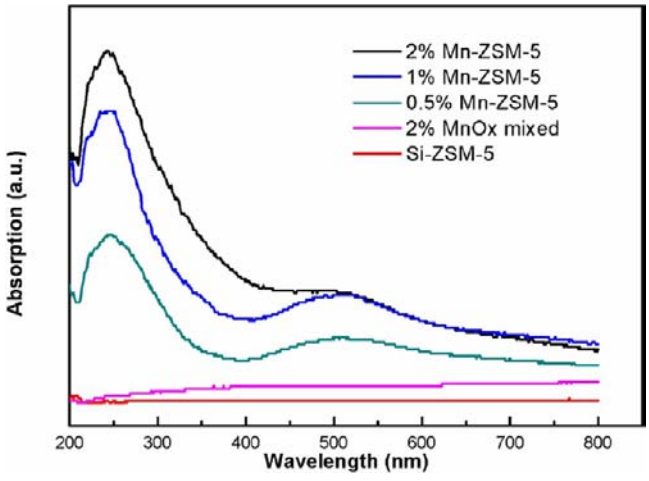

Figure 8. UV−vis spectra of Mn−ZSM-5 (all silica, 0.5%, 1%, and 2%) and physically mixed 2% MnO2 (>99%, Aldrich) with Si−ZSM-5.

absorption increases proportionally and the color of the synthesized material changes from white (no Mn) to pale pink (0.5% and 1% Mn−ZSM-5), to dark pink (2% Mn−ZSM-5). Although the all silica ZSM-5 has no absorption in the 200−800 nm range, two absorption bands, at 250 and 520 nm, have been found for the Mn-containing zeolites. The 250 nm absorption band lies in the UV range and is assigned to electron transfer from O^{2-} to tetrahedral Mn^{3+}, a framework doped Mn ion, with the tail of the band extending to 350 nm because of the extra-framework Mn species present.[17] The broad absorption peak at 520 nm is attributed to d−d transition of either framework or extra-framework Mn^{q+},[35] or possibly surface-associated Mn^{3+}[36] where similar absorbance has been found and shown to have remarkable water oxidation activity.[37]

X-ray Photoelectron Spectroscopy (XPS). XPS was used to analyze both the surface concentration and binding energy of different elements present in the as-synthesized manganese-containing zeolite materials (Figure 9). The O 1s core level spectrum of Si−ZSM-5 showed a main peak at 532.5 eV, which could be ascribed to the binding energy (BE) of oxygen

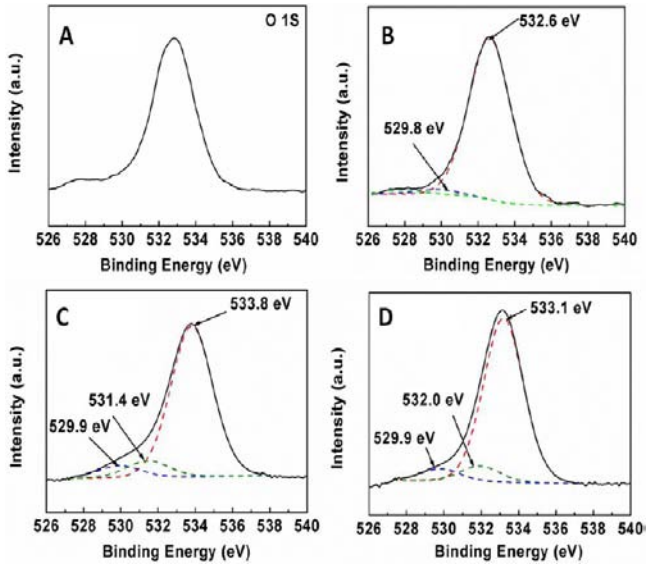

Figure 9. XPS spectra of O 1s region: (A) Si−ZSM-5; (B) 0.5% Mn−ZSM-5; (C) 1% Mn−ZSM-5; (D) 2% Mn−ZSM-5.

belonging to the Si−O bond and is increased to 533.1 eV in the 2% Mn−ZSM-5 sample. Two additional peaks appear in 2% Mn-substituted sample, one at 532.0 eV and the other at 529.9 eV. The BE at the 529.9 eV peak could be ascribed to an oxygen which bonded to Mn (i.e. Mn═O which has a BE around 529.8 eV (Mn(II)O), according to the binding energy database of NIST). The peak at 532.0 eV could be assigned to an oxygen in a framework bonded Mn, i.e. Mn−O−Si. For example, Ti doped in the framework of *r*-MnO_2 material was reported with a peak in the same position and ascribed to the Ti−O−Mn binding.[38] The O 1s spectrum of the 1% Mn sample also showed the identical three distinct peaks, providing reasonable support for the same assignment of the three peaks at 533.8, 531.4, and 529.9 eV, respectively. The Mn 2p core spectrum was obtained from the manganese-containing samples (1 wt % and 2 wt %), providing BEs for Mn $2p_{3/2}$ and Mn $2p_{1/2}$ in these two samples (not shown). For the 1% sample, the binding energies are 643.2 and 654.7 eV, respectively, while those for the 2% sample are 642.1 and 653.5 eV. Although both of the BEs are higher than that for normal MnO_2 because of the strong interaction between manganese and silica, similar results of increased BEs have been reported in other manganese-doped materials or manganese oxides present on the surface of supports.[31]

Thermogravimetric Analysis (TGA). The TGA data in Figure 10 shows the Mn-containing ZSM-5 is as stable as the undoped material without substantial weight loss above 400 °C. Under N_2, the main loss of weight for both the zeolites with and without manganese occurs below 200 °C and is caused by loss of both physically adsorbed water and O_2. The Mn-containing samples showed more apparent weight loss from 200 to 400 °C, compared with the stable undoped one possibly due to the chemical decomposition of the water and oxygen bonded to charge-defective framework sites and surface Mn species. Further weight loss, albeit slight, occurs from 400 to 700 °C, because O_2 evolves from the MnO_x and is proportional to the amount of doped manganese (Figure S4 in SI).

The thermal stability of the synthesized 2% Mn−ZSM-5 material and Si−ZSM-5 were also analyzed by TGA measurements in an O_2 atmosphere. From room temperature to 430

dx.doi.org/10.1021/ja4013936 | J. Am. Chem. Soc. 2013, 135, 8594−8605

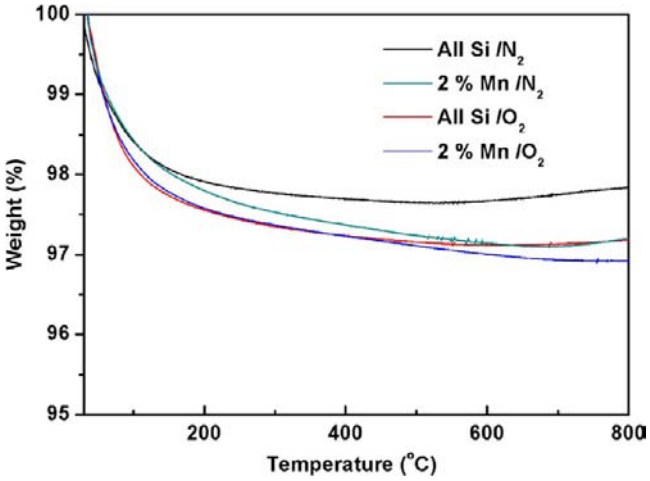

Figure 10. TGA analysis on Si−ZSM-5 and 2% Mn−ZSM-5 under N_2 and O_2 atm.

°C, the weight loss of both materials compares very well, and the loss is mainly from the adsorbed water, whereas from 430 to 800 °C, the 2% Mn−ZSM-5 showed an extra 0.2% weight percent loss, when compared with Si−ZSM-5. On the basis of the 2% Mn loading, 0.2% weight is 10% of the Mn loaded, and this value is right in the line with the weight loss of MnO_2 material because of oxygen evolution, when heated to 800 °C.[39]

Catalytic Results. *1. Toluene Total Oxidation.* The catalytic properties of synthesized Mn−ZSM-5 were tested for gas-phase toluene total oxidation (Figure 11). Generally, the

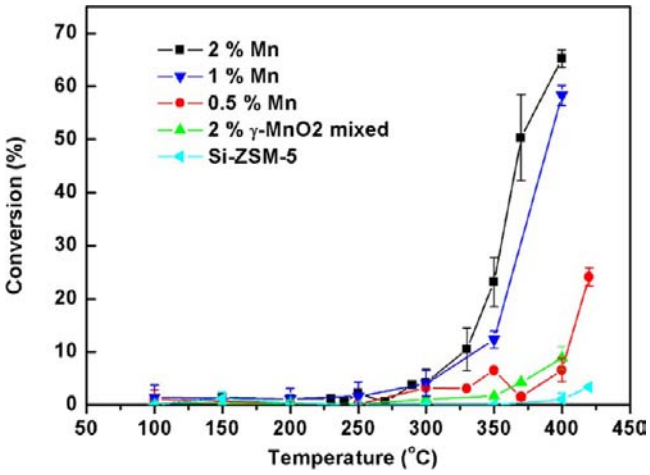

Figure 11. Catalytic activities of toluene total oxidation for Mn−ZSM-5 (all silica, 0.5%, 1%, and 2%), and physically mixed 2% MnO_2 with Si−ZSM-5.

conversion increases when the temperature increases from 300 to 400 °C and above, especially for the Mn-doped samples with high loading (1% and more), showing dramatically increased activity. For example, at 400 °C the conversion increases from 6% to 65% as the loading of Mn increases from 0.5% to 2%, while maintaining 100% selectivity. This should be compared with a 2% γ-MnO_2 physically mixed Si−ZSM-5, used as a reference that shows only 8.8% conversion under the same reaction conditions. Given that Si−ZSM-5 has only 3% conversion even at 420 °C, the considerable activity of the manganese-containing ZSM-5 could be ascribed to the manganese-activated oxygen vacancies as described in our previous research paper on manganese oxide octahedral molecular sieve (OMS-2)-catalyzed VOC oxidation,[20,40] plus the well-dispersed active sites arising from the low dopant amount.[15,35]

2. Gas-Phase Benzyl Alcohol Oxidation. Gas-phase benzyl alcohol oxidation was selected as another probe reaction (Table S1 in SI) which has been investigated by using transition metal-doped metal oxides (e.g., SiO_2, TiO_2) and ZSM-5 as catalysts.[41] For the Si−ZSM-5 material in this study, a relatively low activity, 7.9% as also described in another study, is observed.[41a,d] For the Mn-added samples, the activity is improved to 23.3% at 300 °C. When the temperature increases to 350 °C, the activity of the Mn−ZSM-5 reaches as high as 55%, with a remarkable TOF = 88 h^{-1}. The evidence of the enhanced oxidative property by adding manganese is clearly shown and may be related to the oxygen active sites bonding to the Mn, as revealed from the absorption spectra.

Temperature Programmed Reduction (TPR). CO-TPR was performed on the Si−ZSM-5 and Mn−ZSM-5 (0.5%, 1%, and 2%) samples. The reduction profiles are shown in Figure 12. The reduction occurs only when the temperature exceeds

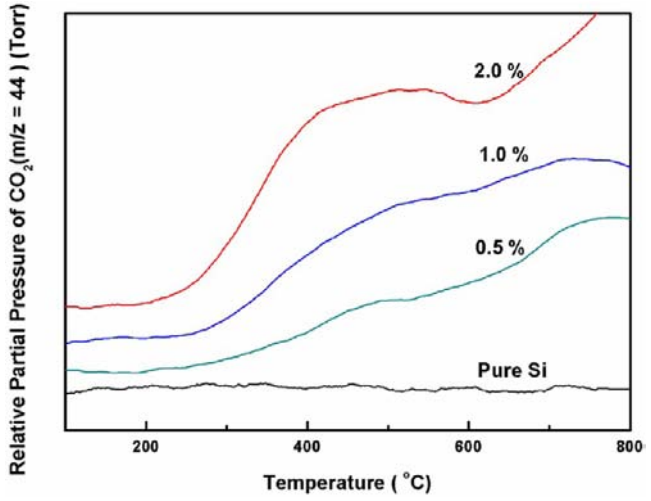

Figure 12. CO-TPR profiles of Mn−ZSM-5 (all silica, 0.5%, 1%, and 2%).

300 °C, further explaining the enhanced activities for toluene oxidation in the same temperature window. There are mainly two reduction peaks for all the Mn-containing zeolites: one lies between 300 −500 °C, while the other falls between 500−800 °C. However, for the sample with 2% Mn, there is a pronounced shift of the intense reduction peak to lower than 400 °C suggesting a better oxidation activity than that of other samples (Figure S6 in SI). The first reduction peak (alpha) is a result of the evolution of adsorbed oxygen on the defective sites. On the other hand, the beta reduction peak is due to the evolution of lattice oxygen, accompanied by a phase transformation from Mn_2O_3 to Mn_3O_4, Mn_3O_4 to MnO, which is in agreement with the results from TGA. Nevertheless, the reduction peak of the 2% sample has the highest intensity, which is related to the amount of Mn in the sample, i.e, the higher the amount of Mn dopant, the higher the reduction intensity (better oxidation activity). All silica ZSM-5 did not show any oxidation activity based on the CO-TPR, which displays an almost flat line. The improvement of the oxidative

dx.doi.org/10.1021/ja4013936 | J. Am. Chem. Soc. 2013, 135, 8594−8605

activity is revealed by an increase of the reduction peak with temperature increase, pushing the front of the reduction curve forward into the lower-temperature region as the amount of Mn increases. The TPR results have confirmed the catalytic activity: 2% > 1% > 0.5% > blank.

DISCUSSION

Ion-Exchange Property and Hydrothermal Stability. The hydrothermal stability and ion-exchange property were characterized by adding 0.2 g of template free 2% Mn−ZSM-5 into 10% NH_4NO_3 water solution, and refluxing for 24 h at 100 °C. Both the structure and morphology do not change after the treatment, suggesting that Mn−ZSM-5 is quite stable under steaming. The Si to Mn ratio does not increase, showing the manganese might be in the zeolite framework and strongly bonded. XRD, SEM, and EDAX measurements of the sample before and after ion exchange are listed in the SI (Figures S7, S8, and S9).

Autoreduction and Oxygen Evolution. Synthesized 2% Mn−ZSM-5 was degassed under 400 °C in the Micromeritics ASAP 2010 for 6 h. The UV−vis spectra were taken before and after this operation. On the basis of Figure 13, the maximum

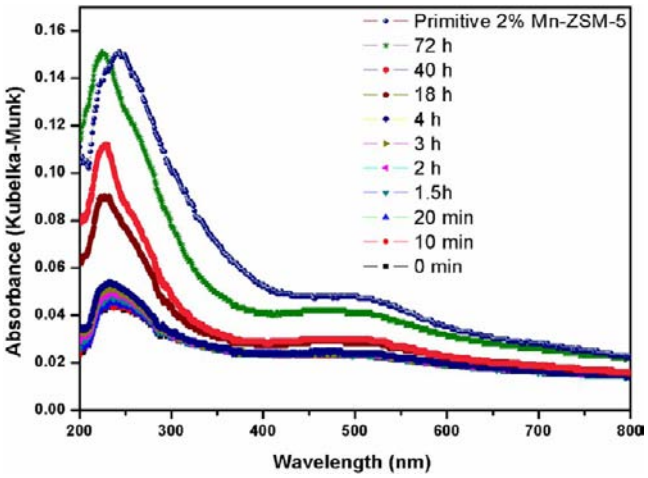

Figure 13. UV−vis absorption spectra of degassed 2% Mn−ZSM-5 after being exposed to air for different periods from 0−72 h along with the absorption of the initial sample before degassing.

absorption at both 250 and 520 nm decreases considerably after degassing and is accompanied by a color change from dark pink to pure white after degassing. When exposed to air, the absorption is restored in 48 h and is also observed from the color of the material returning to dark pink (Figure S10 in SI). The same phenomenon has been found in other transition metal-loaded zeolites.[1] This is the first report for Mn-loaded ZSM-5 zeolites. The autoreduction might be due to the dehydration and desorption of O_2 between the $Mn^{3+}(OH)_x$ sites.[1]

Oxygen evolution is also observed from TGA analysis by comparing the results from N_2 with those from O_2. For the samples run under N_2, the discrepancy of the TGA curves appears at 120 °C and then develops into a major weight loss gap after 400 °C. However, for the samples tested under O_2, there is no significant difference of weight loss until 430 °C. This unambiguous result points to the observation that the difference should come not only from loss of water. Oxygen is evolving from the Mn−ZSM-5 samples, producing the gap at 120 °C. Since there is an excess of O_2 for the O_2-TGA, that result could be balanced with depleted oxygen from the Mn−ZSM-5, because equilibrium is quickly reached between the sample and the O_2 atmosphere. Thus, the gap of the weight loss between pure Si−ZSM-5 and 2% Mn−ZSM-5 is not observed. Nevertheless, under N_2, there is no O_2 in the atmosphere to replenish the depleted vacancy, and the oxygen is released without being replenished. Most importantly, the TGA results agree with our observation of the degassing process and when the sample is activated in air or oxygen. The color change does not take place as in the degassing process due to unchanged bonding between Mn and oxygen. The color change of the material is relevant to the oxygen evolution and may be due to the changing coordination of Mn when the coordinated Mn−O bond is broken, accompanied by novel photoabsorption properties and catalytic properties.[42] The introduction of Mn is crucial to the production of oxidative sites in order to maintain an evolution-replenishing process.

Manganese Substituted in the Zeolite Structure. X-ray diffraction data for the synthesized Si−ZSM-5 and Mn-containing ZSM-5 material show the monoclinic MFI zeolite structure, space group $p2_1/n$. The data are indexed according to a research paper by Artioli et al.[43] The calculated crystal structure data are listed in Table 2.

The size of unit cell increases gradually as the nominal amount of manganese increases (0.5−2%) as reflected by the pronounced expansion of the a, b, and c values and unit cell volume (Figure S11 in SI). However, which of the 0.5% samples are identical to the all-silica sample are probably due to the limited substitution in the framework sites by using less dopants. Moreover, the β value for all the synthesized materials is equal to 90.892, with α and γ equal to 90° which demonstrates a monoclinic crystal structure, rather than orthorhombic, where the α, β, γ values are all equal to 90°. This result agrees with monoclinic lattice parameters published elsewhere.[43,44] In this case, diffraction peaks are split between 8.7 and 9.0° and are assigned to (020) and (200), respectively, while the peak at around 29.9° was assigned to (053) and assumed to be a single peak. The doublets of the peak at 2θ = 24.4° are also typical monoclinic feature. This was further confirmed by matching the selected area electron diffraction (SAED) patterns with a standard MFI-type zeolite made by Artioli et al.,[43] shown in Figure 14.

The enlargement of unit cells could be explained by the substitution of Mn^{3+} in the tetrahedral framework of MFI

Table 2. XRD Lattice Constants a, b, c, and (α, β, γ) for Synthesized Mn−ZSM-5 Materials with a Monoclinic Structure

samples (% Mn−ZSM-5)	a	b	c	α	β	γ
0	19.82	20.08	13.35	90.00	90.89	90.00
0.5	19.82	20.08	13.35	90.00	90.89	90.00
1	19.84	20.10	13.36	90.00	90.89	90.00
2	19.91	20.16	13.40	90.00	90.89	90.00

dx.doi.org/10.1021/ja4013936 | J. Am. Chem. Soc. 2013, 135, 8594−8605

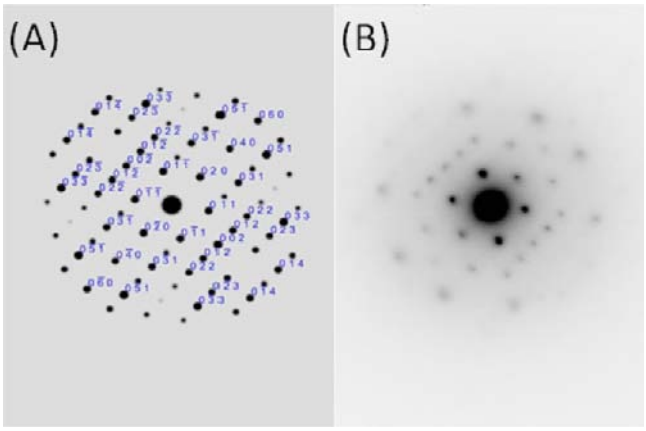

Figure 14. Match of (A) standard diffraction pattern for monoclinic-MFI zeolite with (B) SAED pattern from experiment (Figure 5A, inset), both patterns orientated along the [010] plane.

zeolite, which involves an absorption at 250 nm as a result of charge transfer from O^{2-} to Mn^{3+} in tetrahedral coordination. On the other hand, no absorption occurred for either the non-Mn-containing samples or the commercial manganese oxides which are octahedrally coordinated. Besides, there is broad absorption around 500 nm for all manganese-containing samples, which is assigned to $^6A_{1g}$ to $^4T_{2g}$ crystal field transitions of Mn^{2+} as described in other Mn-containing zeolite materials.[35] This could be attributed to the Mn^{2+} species bonded on the surface of ZSM-5 and may explain the color of the material. The substitution of Mn in the ZSM-5 structure was also indicated by the shift of Raman peaks of the 5-membered ring vibrations of MFI-type zeolite. A slight shift of the peak at 380 cm^{-1} to lower wave numbers means weakened Si−O bonds as the amount of Mn increases without showing extra peaks due to Mn−O vibrations until the amount of Mn increased to 2 wt %. The increasing absorption of UV−visible light, the red shift of the Raman spectra, and the increase of lattice parameters all provide strong evidence for the incorporation of Mn in the zeolite framework occurring during the synthesis.

Amorphous Manganese Species on the Surface. On the basis of the X-ray diffraction data, there are no crystalline manganese oxide phases in all the manganese-containing materials, but clear evidence that extra Mn-containing phases exists on the surface is shown by UV−vis and Raman, as well as XPS.

The broad UV−vis absorption peak at 500 nm represents the possible existence of Mn^{2+} on the surface of Mn−ZSM-5 material. The same phenomenon has been observed for the Mn-containing MCM-41 zeolite material prepared by a similar direct hydrothermal synthesis.[45] Nevertheless, the Raman spectroscopy provided direct evidence of the occurrence of MnO_x species on the surface. The new peak centered at 560 cm^{-1} was assigned to symmetric stretching of the Mn−O−Si in the framework, whereas the band at 628 cm^{-1} could be ascribed to surface manganese species from manganese substitution of surface-bonded OH groups. Similar results have been reported for Mn−MCM-41 and silica-supported manganese oxides.[31,45] Raman spectra taken from different micrometer-sized particles (assisted by high-resolution microscopy) have shown a pronounced different relative intensity of multiple vibration bands which further confirms the inhomogeneous property of the high-loading Mn−ZSM-5 (2%), probably caused by the unevenly distributed Mn surface-bonding species. Surface manganese is also suggested by XPS results, as the assignment of a deconvoluted peak at about 529.7−529.9 eV shows, with an increasing ratio from 2.92% in the 0.5% Mn to 6.2% in the 2% Mn sample, and a comparable ratio of 6.57% in the 1% sample, when the total oxygen bonding is considered as a unit.

Highly Selective Catalytic Properties. The redox activity of the Mn-doped zeolites was studied by both catalytic gas-phase benzyl alcohol oxidation and toluene total oxidation. The catalysts are active and selective for both reactions but in different temperature ranges. For the benzyl alcohol oxidation, the feasible temperature range for catalytic activity is between 300 and 350 °C, in which the benzyl alcohol was selectively converted to benzaldehyde. Complete oxidation was found when the temperature increased to 400 °C by detecting abundant carbon dioxide in the gas-phase products. More than 50% yield was achieved at 350 °C with 80% selectivity. The TOF number is as high as 88 h^{-1} by considering Mn as the only active sites (SI). The total oxidation for benzyl alcohol which occurs at temperatures higher than 350 °C is undesirable, but if applied as a catalyst for toluene conversion, then this process affords total oxidation. This assumption was realized by running the Mn-containing ZSM-5 in a gas-phase toluene oxidation system, with undoped Si−ZSM-5 as a blank and 2% MnO_2 physically mixed blank as a control. The experimental results showed that the synthesized Mn-containing zeolite is much more active than both the physically mixed sample and the blank. The 2% Mn−ZSM-5 showed 65% conversion and 100% selectivity of carbon dioxide at 400 °C compared with the blank which had less than 1% conversion under the same conditions. The proportional increase in activity as a concomitant increase in the amount of Mn added provides validity for the redox activity of manganese introduced by one-step synthesis.

Comparison of Experiments and Calculations. The performance of Mn−ZSM-5-doped zeolites depends strongly on the Mn environment. The XRD data given above reveals that the unit cell volume increases linearly with increasing Mn leading to the supposition of isomorphous substitution of Mn at tetrahedral framework sites. Since Mn^{3+} is more inclined than Mn^{2+} to be substituted for Si^{4+}, part of the manganese ions may be incorporated into the framework of ZSM-5 preferentially as Mn^{3+}. On the other hand, it is also possible to have Mn species located at extra-framework positions as either Mn^{2+}, Mn^{3+}, or possibly Mn^{4+} ions. UV−vis spectroscopy is one of the most useful tools to study the locale of the Mn^{q+} environment where electronic spectra show various types of absorptions including d → d transitions on the manganese ion, ligand-to-metal charge transfer from the oxygen to the manganese, LMCT, (Mn^{3+} O^{2-} → Mn^{2+} O^{-}) transitions, and perhaps ligand−ligand (L → L) transitions. The wavelengths at which various transitions occur can be highly sensitive to the local environment of the Mn ion and can serve as a probe for determining the Mn coordination. The experimental UV−vis absorption spectra shown in Figures 8 and 13 are similar to those obtained previously in several past experiments.[46]

The results presented here aim to establish a correlation between the experimental UV−vis absorption spectra on Mn-containing samples and the calculated photophysical properties calculated using time-dependent density functional theory (TD-DFT). All the simulated spectra presented here are obtained with the SpecDis[47] program using a lifetime broadening of Γ = 0.16 eV, i.e. full width at half-maximum (fwhm).

dx.doi.org/10.1021/ja4013936 | J. Am. Chem. Soc. 2013, 135, 8594−8605

Structure of Model $Mn(OSiH_3)_4^-$ Compound and Embedded Mn−Zeolite Cluster. Optimized geometry parameters for the D_{2d} $Mn(OSiH_3)_4^-$ model compound and the embedded Mn-$(O\text{-}SiH_2\text{-})_4$, primary structure (PS), are given in Table 3.

Table 3. Optimized Geometric Parameters for the $Mn(OSiH_3)_4^-$ Model Compound and Embedded Mn-$(O\text{-}SiH_2\text{-})_4^-$ Primary Structure (PS) of Mn−ZSM-5

	geometric parameters	
	$Mn(OSiH_3)_4^-$	PS of Mn−ZSM-5
Mn−O	1.86 Å	1.86 Å
Si−O	1.63 Å	1.62 Å
O−Mn−O	135°	107°
O−Mn−Si	136°	140°

Table 3 shows that the Mn−O and Si−O distances as well as the O−Mn−Si angles in both the $Mn(OSiH_3)_4^-$ model compound and Mn-$(O\text{-}SiH_2\text{-})_4$ primary structure are in very good agreement. However, the O−Mn−O angle is more open in the $Mn(OSiH_3)_4^-$ model compound because there is a lack of constraining forces, and the UFF parameters used for Mn in the QM/MM calculation were defined for octahedral Mn^{2+} which would lead to smaller O−Mn−O angles.

Spectra of Model $Mn(OSiH_3)_4^-$ Compound and Embedded Mn−Zeolite Cluster. Simulated UV−vis spectra for the model compound and the embedded Mn−zeolite cluster model are given for $Mn(OSiH_3)_4^-$ in Figure 15 which

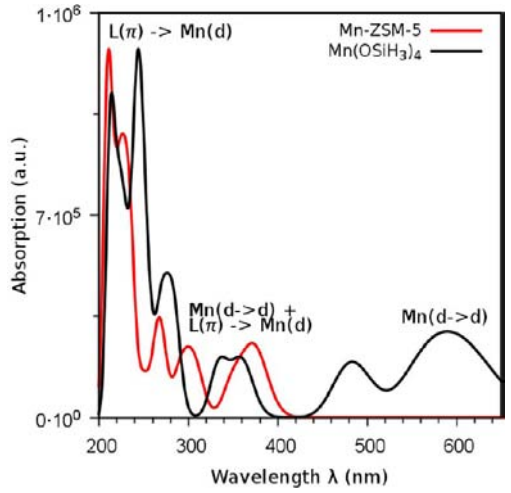

Figure 15. Simulated UV−vis spectra of the model $Mn(OSiH_3)_4^-$ compound and an Mn ion inserted into the zeolite framework.

also provides a comparison of the calculated spectra for these two model compounds. The calculated UV−vis spectrum of the $Mn(OSiH_3)_4^-$ model compound in Figure 15 is in good agreement with the experimental spectra given in Figures 8 and 13. These data show a peak at about 500 nm which is a result of a Mn (d → d) transition, and is often attributed to surface MnO_y^{x-} products which might also be present.

However, it is possible that all peaks in the experimental spectra come from framework Mn ions embedded in a tetrahedral environment. The peak shown at the shorter wavelength region, 300−450 nm is due to transitions that have both Mn (d → d) and ligand (π → Mn(d)) character to the wave function. Finally, the highest-energy peak in the region of 200−280 nm is the result of metal−ligand charge transfer (MLCT) electronic transitions of the type, Mn^{3+} O^{2-} → Mn^{2+} O^-. The low-energy peak in the 500−600 nm range is missing from the spectrum of the Mn-embedded zeolite cluster shown in Figure 15. The O−Mn−O angle is more constrained to a smaller value in the Mn-embedded zeolite cluster compared to that in the $Mn(OSiH_3)_4^-$ model compound, caused both by the restraining effect of the surrounding zeolite framework and by the lack of UFF parameters for four-coordinate Mn^{3+}. Thus, the interaction of O π orbitals with Mn d orbitals is attenuated as the O−Mn−O angle decreases, causing the d orbital splitting to increase with a concomitant increase in d−d excitation energy.

Calculated Spectra of Manganese Oxides. The existence of manganese oxide species on the surface on Mn−ZSM-5 zeolites is a thorny problem that is difficult to understand clearly. As discussed earlier, the 500 nm absorption peak obtained with diffuse reflectance spectroscopy seems to indicate the presence of either Mn^{2+} or Mn^{3+} on the surface of the Mn−ZSM-5 material. However, the calculated electronic absorption spectrum of $Mn(OSiH_3)_4^-$ as a model for a framework Mn ion does indeed have a transition energy in the 500 nm range. Nevertheless, it may be also possible to have species containing Mn ions located at extra-framework positions which are capable of yielding a peak at 500 nm. It becomes interesting to investigate the absorption spectra of related model manganese oxide anions to determine whether their existence is possible on the Mn−ZSM-5 surface. The calculated absorption spectra of six-coordinate MnO_6^{10-} (Mn(II)) and MnO_6^{9-} (Mn(III)) model compounds are given in Figure 16.

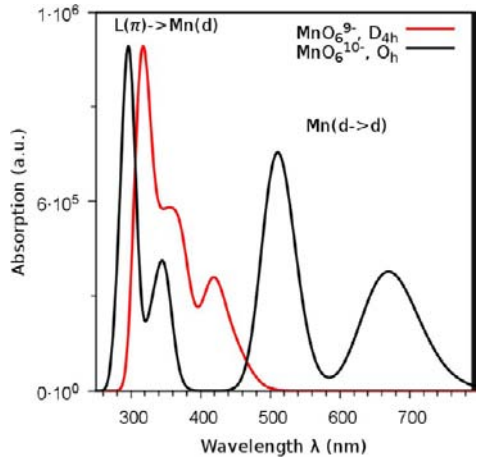

Figure 16. Simulated UV−vis spectra of the six-coordinate MnO_6^{10-}, Mn(II) and MnO_6^{9-}, Mn(III) model oxides. For the Mn^{2+} (d_5) oxide, an Mn−O distance of 2.00 Å with O_h symmetry was used, while the Mn^{3+} (d_4) oxide was tetragonally distorted to D_{4h} symmetry, having distances of $Mn-O_{axial}$ = 2.20 Å and $Mn-O_{equatorial}$ = 2.00 Å.[48].

One striking feature of the calculated spectra presented in Figure 16 is the absence of an absorption peak at 250 nm as shown in Figures 8 and 13 which demonstrates with reasonable certainty that the 250 nm absorption feature is not due to six-coordinate surface oxides. The peaks at 500−700 and 300 nm have been also observed experimentally[48b,49] and provide additional confidence in the calculated absorption spectra. Similar results were also obtained for high-oxidation state, four-coordinate manganese oxides.

dx.doi.org/10.1021/ja4013936 | J. Am. Chem. Soc. 2013, 135, 8594−8605

CONCLUSION

In summary, we have shown a facile synthesis of Mn-containing high silica ZSM-5 zeolite in a single step with concomitant novel optical absorption and catalytic properties. The manganese substituted in the zeolite framework was proven by XRD refinements showing enlarged lattice parameters consistent with the increasing amounts of manganese. Multiple spectroscopic techniques IR, Raman, and UV−visible absorption, as well as elemental analysis such as XPS and EDXS suggested the coexistence of both framework Mn sites and a possible foreign phase, depending on the amount of dopants. In addition, we performed TD-DFT calculations on excited states to simulate the photophysical properties of Mn-containing zeolites for the first time by building model compounds (e.g., $H_3Si{-}O^-$) in four- and six-fold coordination to Mn−O bonding; Mn containing clusters in zeolites were also built, which considered crystal constraints practically. Simulated spectra correlate with the experimental UV−visible absorption reasonably well. Therefore, the validity of Mn-containing zeolites is strengthened from both experimental and theoretical aspects. Theoretical studies were also extended to simulate the absorption of manganese ions in four- and six-fold coordination. Absence of absorption for the six coordinated $[Mn(II/III)O_6]^{10-/9-}$ species at 250 nm suggest the validity of Mn^{3+} in tetrahedral framework sites, yet their presence as surface species cannot be ruled out due to a strong absorption at 500 nm (e.g., $[Mn(II)O_6]^{10-}$). The variable coordination of the Mn bonding with oxygen in the Mn−ZSM-5 showed novel color-changing properties with varying the oxygen atmosphere to an inert atmosphere. However, the system maintained a comparably stable oxidative property by a tentative oxygen depletion and replenishing mechanism under oxygen as supported by TGA and TPR data. Finally, for the first time this Mn−ZSM-5 has shown remarkable activity in catalyzing both benzyl alcohol oxidation and toluene oxidation. This combined experimental and modeling study opens up a new way to design and identify TM-doped zeolites and provides solid evidence for potential applications in heterogeneous catalysis.

ASSOCIATED CONTENT

Supporting Information

Figures S1−S11 and Table S1. This material is available free of charge via the Internet at http://pubs.acs.org.

AUTHOR INFORMATION

Corresponding Author

steven.suib@uconn.edu

Notes

The authors declare no competing financial interest.

ACKNOWLEDGMENTS

We thank Dr. Ray Joesten for help in analyzing the XRD and TEM results, Dr. Heng Zhang (Institute of Material Science) who helped us with the XPS, and Dr. Frank Galasso for many helpful discussions. This work was supported by the U.S. Department of Energy, Office of Basic Energy Sciences, Division of Chemical, Geochemical and Biological Sciences under Contract DE-FG02-86ER13622.A000.

REFERENCES

(1) Smeets, P. J.; Woertink, J. S.; Sels, B. F.; Solomon, E. I.; Schoonheydt, R. A. *Inorg. Chem.* **2010**, *49*, 3573−3583.
(2) Hammond, C.; Forde, M. M.; Ab Rahim, M. H.; Thetford, A.; He, Q.; Jenkins, R. L.; Dimitratos, N.; Lopez-Sanchez, J. A.; Dummer, N. F.; Murphy, D. M.; Carley, A. F.; Taylor, S. H.; Willock, D. J.; Stangland, E. E.; Kang, J.; Hagen, H.; Kiely, C. J.; Hutchings, G. J. *Angew. Chem., Int. Ed.* **2012**, *51*, 5129−5133.
(3) Corma, A.; García, H. *Chem. Rev.* **2002**, *102*, 3837−3892.
(4) Chen, L.-H.; Li, X.-Y.; Tian, G.; Li, Y.; Rooke, J. C.; Zhu, G.-S.; Qiu, S.-L.; Yang, X.-Y.; Su, B.-L. *Angew. Chem., Int. Ed.* **2011**, *50*, 11156−11161.
(5) Li, C.; Xiong, G.; Liu, J.; Ying, P.; Xin, Q.; Feng, Z. *J. Phys. Chem. B* **2001**, *105*, 2993−2997.
(6) Ko, Y.; Kim, S. J.; Kim, M. H.; Park, J.-H.; Parise, J. B.; Uh, Y. S. *Microporous Mesoporous Mater.* **1999**, *30*, 213−218.
(7) Maschmeyer, T.; Rey, F.; Sankar, G.; Thomas, J. M. *Nature* **1995**, *378*, 159−162.
(8) Guo, B.; Zhu, L.; Hu, X.; Zhang, Q.; Tong, D.; Li, G.; Hu, C. *Catal. Sci. Technol.* **2011**, *1*, 1060−1067.
(9) Tao, Y.; Lita, A.; van de Burgt, L. J.; Zhou, H.; Stiegman, A. E. *Inorg. Chem.* **2012**, *51*, 2432−2437.
(10) Lita, A.; Tao, Y.; Ma, X.; van de Burgt, L.; Stiegman, A. E. *Inorg. Chem.* **2011**, *50*, 11184−11191.
(11) (a) Suib, S. L. *Acc. Chem. Res.* **2008**, *41*, 479−487. (b) Suib, S. L. *J. Mater. Chem.* **2008**, *18*, 1623−1631. (c) Son, Y.-C.; Makwana, V. D.; Howell, A. R.; Suib, S. L. *Angew. Chem., Int. Ed.* **2001**, *113*, 4410−4413. (d) Luo, J.; Zhang, Q.; Huang, A.; Suib, S. L. *Microporous Mesoporous Mater.* **2000**, *35*, 209−217.
(12) Yang, Z.-Z.; Deng, J.; Pan, T.; Guo, Q.-X.; Fu, Y. *Green Chem.* **2012**, *14*, 2986−2989.
(13) Davis, M. E.; Lobo, R. F. *Chem. Mater.* **1992**, *4*, 756−768.
(14) Lita, A.; Ma, X.; Meulenberg, R. W.; van Buuren, T.; Stiegman, A. E. *Inorg. Chem.* **2008**, *47*, 7302−7308.
(15) Tusar, N. N.; Jank, S.; Glaser, R. *ChemCatChem* **2011**, *3*, 254−269.
(16) Round, C. I.; Williams, C. D.; Duke, C. V. A. *Chem. Commun.* **1997**, 1849−1850.
(17) Xin, H.; Zhao, J.; Xu, S.; Li, J.; Zhang, W.; Guo, X.; Hensen, E. J. M.; Yang, Q.; Li, C. *J. Phys. Chem. C* **2010**, *114*, 6553−6559.
(18) Tušar, N. N.; Logar, N. Z.; Arčon, I.; Thibault-Starzyk, F.; Ristić, A.; Rajić, N.; Kaučic, V. *Chem. Mater.* **2003**, *15*, 4745−4750.
(19) Flanigen, E. M.; Bennett, J. M.; Grose, R. W.; Cohen, J. P.; Patton, R. L.; Kirchner, R. M. *Nature* **1978**, *271*, 512−516.
(20) Genuino, H. C.; Dharmarathna, S.; Njagi, E. C.; Mei, M. C.; Suib, S. L. *J. Phys. Chem. C* **2012**, *116*, 12066−12078.
(21) Frisch, M. J.; Trucks, G. W.; Schlegel, H. B.; Scuseria, G. E.; Robb, M. A.; Cheeseman, J. R.; Scalmani, G.; Barone, V.; Mennucci, B.; Petersson, G. A.; Nakatsuji, H.; Caricato, M.; Li, X.; Hratchian, H. P.; Izmaylov, A. F.; Bloino, J.; Zheng, G.; Sonnenberg, J. L.; Hada, M.; Ehara, M.; Toyota, K.; Fukuda, R.; Hasegawa, J.; Ishida, M.; Nakajima, T.; Honda, Y.; Kitao, O.; Nakai, H.; Vreven, T.; Montgomery, J. A., Jr.; Peralta, J. E.; Ogliaro, F.; Bearpark, M.; Heyd, J. J.; Brothers, E.; Kudin, K. N.; Staroverov, V. N.; Kobayashi, R.; Normand, J.; Raghavachari, K.; Rendell, A.; Burant, J. C.; Iyengar, S. S.; Tomasi, J.; Cossi, M.; Rega, N.; Millam, J. M.; Klene, M.; Knox, J. E.; Cross, J. B.; Bakken, V.; Adamo, C.; Jaramillo, J.; Gomperts, R.; Stratmann, R. E.; Yazyev, O.; Austin, A. J.; Cammi, R.; Pomelli, C.; Ochterski, J. W.; Martin, R. L.; Morokuma, K.; Zakrzewski, V. G.; Voth, G. A.; Salvador, P.; Dannenberg, J. J.; Dapprich, S.; Daniels, A. D.; Farkas, M.; Foresman, J. B.; Ortiz, J. V.; Cioslowski, J.; Fox, D. J., *Gaussian 09*, Revision A.02; Gaussian Inc.: Wallingford CT: 2009.
(22) *GAMESS*, Version 1, May 2012 (R1) as originally cited in Schmidt, M. W.; Baldridge, K. K.; Boatz, J. A.; Elbert, S. T.; Gordon, M. S.; Jensen, J. H.; Koseki, S.; Matsunaga, N.; Nguyen, K. A.; Su, S. J.; Windus, T. L.; Dupuis, M.; Montgomery, J. A., Jr. *J. Comput. Chem.* **1993**, *14*, 1347−1363.
(23) (a) Bauernschmitt, R.; Ahlrichs, R. *Chem. Phys. Lett.* **1996**, *256*, 454−464. (b) Rinkevicius, Z.; Vahtras, I.; Ågren, H. *J. Chem. Phys.* **2010**, *133*, 114104−114116. (c) Bernard, Y.; Shiao, Y.; Krylov, A. *J. Chem. Phys.* **2012**, *136*, 204103−204120.

(24) (a) Lee, C.; Yang, W.; Parr, R. *Phys. Rev. B* **1988**, *37*, 785−790. (b) Becke, A. D. *Phys. Rev. B* **1988**, *38*, 3098−3100. (c) Casida, M.; Jamorski, C.; Casida, K.; Salahub, D. *Chem. Phys. Lett.* **1998**, *108*, 4439−4449.
(25) Hay, P.; Wadt, W. *J. Chem. Phys.* **1985**, *82*, 270−283.
(26) Ditchfield, R.; Hehre, W.; Pople, J. A. *J. Chem. Phys.* **1971**, *54*, 724.
(27) (a) Dapprich, S.; Komaromi, I.; Byun, K.; Morokuma, K.; Frisch, M. *J. Mol. Struct. (THEOCHEM)* **1999**, *462*, 1−21. (b) Vreven, T.; Morokuma, K.; Farkas, O.; Schlegel, H.; Frisch, M. *J. Chem. Theory Comput.* **2003**, *24*, 760−769.
(28) (a) Schäfer, A.; Horn, C.; Ahlrichs, R. *J. Chem. Phys.* **1992**, *97*, 2571−2577. (b) Schäfer, A.; Huber, C.; Ahlrichs, R. *J. Chem. Phys.* **1994**, *100*, 5829−5835.
(29) Rappe, A.; Casewit, C.; Colwell, K.; Goddard, W.; Skiff, W. *J. Am. Chem. Soc.* **1992**, *114*, 10024−10035.
(30) Kapteijn, F.; van Langeveld, A. D.; Moulijn, J. A.; Andreini, A.; Vuurman, M. A.; Turek, A. M.; Jehug, J.-M.; Wachs, I. E. *J. Catal.* **1994**, *150*, 94−104.
(31) Fabrizioli, P.; Buŕgi, T.; Baiker, A. *J. Catal.* **2002**, *207*, 88−100.
(32) Smeets, P. J.; Hadt, R. G.; Woertink, Julia S.; Vanelderen, P.; Schoonheydt, R. A.; Sels, B. F.; Solomon, E. I. *J. Am. Chem. Soc.* **2010**, *132*, 14736−14738.
(33) Solomon, E. I.; Ginsbach, J. W.; Heppner, D. E.; Kieber-Emmons, M. T.; Kjaergaard, C. H.; Smeets, P. J.; Tian, L.; Woertink, J. S. *Faraday Discuss.* **2011**, *148*, 11−39.
(34) Zecchina, A.; Bordiga, S.; Spoto, G.; Marchese, L.; Petrini, G.; Leofanti, G.; Padovan, M. *J. Phys. Chem.* **1992**, *96*, 4985−4990.
(35) Kijlstra, W. S.; Poels, E. K.; Bliek, A.; Weckhuysen, B. M.; Schoonheydt, R. A. *J. Phys. Chem. B* **1997**, *101*, 309−316.
(36) Radu, D.; Glatzel, P.; Gloter, A.; Stephan, O.; Weckhuysen, B. M.; de Groot, F. M. F. *J. Phys. Chem. C* **2008**, *112*, 12409−12416.
(37) Takashima, T.; Hashimoto, K.; Nakamura, R. *J. Am. Chem. Soc.* **2012**, *134*, 18153−18156.
(38) Jin, L.; Xu, L.; Morein, C.; Chen, C.-h.; Lai, M.; Dharmarathna, S.; Dobley, A.; Suib, S. L. *Adv. Funct. Mater.* **2010**, *20*, 3373−3382.
(39) Kingondu, C. K.; Opembe, N.; Chen, C. H.; Ngala, K.; Huang, H.; Iyer, A.; Garcés, H. F.; Suib, S. L. *Adv. Funct. Mater.* **2011**, *21*, 312−323.
(40) Mukri, B. D.; Dutta, G.; Waghmare, U. V.; Hegde, M. S. *Chem. Mater.* **2012**, *24*, 4491−4502.
(41) (a) Biella, S.; Rossi, M. *Chem. Commun.* **2003**, 378−379. (b) Yamamoto, R.; Sawayama, Y.; Shibahara, H.; Ichihashi, Y.; Nishiyama, S.; Tsuruya, S. *J. Catal.* **2005**, *234*, 308−317. (c) Fan, J.; Dai, Y.; Li, Y.; Zheng, N.; Guo, J.; Yan, X.; Stucky, G. D. *J. Am. Chem. Soc.* **2009**, *131*, 15568−15569. (d) Hayashibara, H.; Nishiyama, S.; Tsuruya, S.; Masai, M. *J. Catal.* **1995**, *153*, 254−264.
(42) Soo, H. S.; Macnaughtan, M. L.; Weare, W. W.; Yano, J.; Frei, H. *J. Phys. Chem. C* **2011**, *115*, 24893−24905.
(43) Artioli, G.; Lambertib, C.; Marra, G. L. *Acta Crystallogr., Sect. B* **2000**, *56*, 2−10.
(44) van Koningsveld, H.; Jansen, J. C.; van Bekkum, H. *Zeolites* **1990**, *10*, 235−242.
(45) Zhang, Q.; Wangb, Y.; Itsuki, S.; Shishido, T.; Takehira, K. *J. Mol. Catal. A: Chem.* **2002**, *188*, 189−200.
(46) (a) Kijlstra, W.; Poels, E. K.; Blick, A.; Weckhuysen, B. M.; Schoonheydt, R. A. *J. Phys. Chem. B* **1997**, *101*, 309−316. (b) Velu, S.; Shah, N.; Jyothi, T. M.; Sivasanker, S. *Microporous Mesoporous Mater.* **1999**, *33*, 61−75. (c) Zhang, Q.; Yang, Y.; Itsuki, S.; Shishido, T.; Takehira, K. *J. Mol. Catal. A: Chem.* **2002**, *188*, 189−200. (d) Radu, D.; Glatzel, P.; Gloter, A.; Stephan, O.; Weckhuysen, B. M.; de Groot, F. *J. Phys. Chem. C* **2008**, *112*, 12409−12416. (e) Tang, Q.; Hu, S.; Chen, Y.; Guo, Z.; Chen, Y.; Yang, Y. *Microporous Mesoporous Mater.* **2010**, *132*, 501.
(47) Bruhn, T.; Schaumlöffel, A.; Hemberger, Y.; Bringmann, G. *SpecDis*, Version 1.60; University of Würtzburg: Germany, 2012.
(48) (a) Sherman, D. M. *Am. Mineral.* **1984**, *69*, 788−799. (b) Sherman, D. M.; Vergo, N. *Am. Mineral.* **1988**, *73*, 140−144.
(49) (a) Thauern, H.; Glaum, R. *Inorg. Chem.* **2007**, *46*, 2057−2066. (b) Langer, K.; Abu-Eid, R. *Phys. Chem. Miner.* **1977**, *1*, 273−299. (c) Pratt, G. W., Jr.; Coelho, R. *Phys. Rev.* **1959**, *116*, 281−286.